RSC Advances

ROYAL SOCIETY OF CHEMISTRY

www.rsc.org/advances

Journal Name

ARTICLE TYPE

Cite this: DOI: 10.1039/xxxxxxxxxx

Multi-scale simulation of non-equilibrium phase transition under shear flow in dilute polymer solutions

Xin-Hai Xu,[a] Xiao-Wei Guo,[a*] Yu Cao,[a] Xiao-Guang Ren,[a] Juan Chen, [a] and Xue-Jun Yang[a]

Received Date
Accepted Date

DOI: 10.1039/xxxxxxxxxx

www.rsc.org/journalname

The phase transition of complex fluids is intrinsically a multi-scale problem. In this paper we proposed a multi-scale two-fluid model, that couples a coarse-grained microscopic method to the two-fluid framework for studying the multi-phase fluids under shear flow. In this model the macroscopic viscoelastic stress is calculated by tracking massive microscopic Brownian configuration fields in the simulation box. Both of the macroscopic and the microscopic equations are solved using a modified PISO iterative algorithm based on finite volume discretization scheme. Our 2D numerical results reproduce numerous dynamic phenomena reported in literature and show that the theoretical model presented here could be a possible multi-scale approach to numerically study the multi-phase viscoelastic fluids under flow.

1 Introduction

Phase separation is a fundamental phenomenon that is commonly observed in complex fluids. Driven by the thermodynamical and the viscoelastic forces, the system can produce spatially heterogeneous patterns. After the experimental result presented by Silberberg [1] showing that the phase transitions of polymer solutions can be strongly influenced by flow, there have been numerous reports on the shear-induced phase separation in complex fluids [2–5]. Typically, the morphology of the field will form into band structures under shear flow. As a closely related phenomenon, the shear-banded flows also have been widely studied. The reader interested in the shear-banding and its relations to the phase separation under shear flows may refer to the four review papers [6–9].

Although most of the numerical study of the shear-induced phase transition considered the system in a thermal-equilibrium state, most systems found in nature are not in such an ideal state. In this paper we focused on the non-equilibrium phase separation under shear flow. In classical binary fluids, the spinodal decomposition will occur after a temperature quench without flow. This non-equilibrium phase separation has been well understood through numerous early experimental [10–14] and numerical [15–17] research. Additionally, a number of intriguing effects induced by shear were observed, typical results included the highly elongated domains in very weak shear and a string phase in steady state under strong shear. For colloidal systems under shear the reader could refer to the review paper by Lowen [18]. Stansell's group [19,20] provided convincing evidences for the non-equilibrium steady states through numerical simulation. Fielding [21] presented an in-depth numerical study on the role of inertia in non-equilibrium steady states and confirmed that the nonequilibrum steady states free of finite-size effects only existed in the systems with inertia.

Theoretically, modeling the phase transition under flow involves the thermodynamics, hydrodynamics and the viscoelastic effects. For simplicity, most of the previous study about the non-equilibrium phase transition adopted a simple model ignoring the viscoelastic effects. As a macroscopic approach, the two fluid model [22–25] was widely used to investigate the phase separation in viscoelastic fluids. Numerous extensions [26–29] of the original two-fluid model was proposed recently and the results revealed that the model could capture the essential features of the viscoelastic phase separation. The two-fluid theoretical framework could be used to replace the previous simple models [19–21] for studying the non-equilibrium viscoelastic phase separation.

Compared with the classical viscous fluids, predicting the flow characteristics of a complex fluid is much more difficult since the macroscopic viscoelastic stress is determined by the complex microscopic dynamics of molecular chains. That means intrinsically the phase transition of complex fluids is a multi-scale problem. The atomistic modelling is the most detailed approach to describe the rheological behaviour in complex fluids, however, considering the massive computer resource requirement, this microscopic approach is limited to flow geometries of molecular dimensions. Thus some micro-macro methods [30] were introduced that coupled the coarse-grained molecular kinetic theory to the macroscopic

[a] State Key Laboratory of High Performance Computing, National University of Defense Technology, China
*Corresponding author: guoxiaowei@nudt.edu.cn
† Electronic Supplementary Information (ESI) available: [details of any supplementary information available should be included here]. See DOI: 10.1039/b000000x/

continuum equations. The Brownian configuration field (BCF) method proposed by Hulsen et al.[31] is a promising new multi-scale approach to model the viscoelastic fluids. The key idea of the BCF method is using Brownian configuration fields instead of tracking discrete particles, and that significantly reduces the drawbacks of the CONNFFESSIT method introduced by Laso and Ottinger[32]. In practice the BCF method works very well and has been applied to simulation of numerous viscoelastic flows, including the flow past a cylinder[31,33], viscoelastic free surface flows[34], contraction and expansion flows[35], Couette flow, Poiseuille flow, lid driven cavity flow[36] and flow between eccentrically rotating cylinders[37]. Due to the spatial smoothness, the BCF method has a considerable increased numerical stability. This advantage was confirmed in previous research and Mangoubi[38] recently gave an in-depth analysis about the origin of the numerical stability of the BCF method.

As a multi-scale approach, the BCF method requires much more computational resources compared to purely macroscopic approaches, both for CPU time and memory. Therefore, most simulations based on BCF method are by now restricted to 2D spaces and homogeneous flow fields. The most largest scale of BCF simulation was presented by Griebel and Ruttgers[39], in this study they gave the first 3D multi-scale FENE simulations using the BCF approach for square-square contraction flows. Nevertheless, to our best knowledge, there is so far no applications of the BCF approach for simulations of viscoelastic phase transition in complex fluids.

In this paper, we couple the BCF approach into the two-fluid framework and numerically solve this multi-scale two-fluid model through finite volume method. We mainly focus on the 2D simulation results of non-equilibrium phase separation phenomenon in dilute polymer solutions.

The remainder of the paper is organized as follows. In the next section the governing equations of a multi-scale two-fluid model are presented and the numerical algorithms for solving the equations are describes in Section 2. Followed by the simulation results and discussions in Section 4, Section 5 contains our conclusions.

2 A multi-scale two-fluid model

For modeling the multi-phase fluid dynamics of a dilute polymer solution, we propose a multi-scale approach derived from the two-fluid concept and couple the Brownian Configuration Fields (BCF) method for computing the viscoelastic stress. The governing equations are divided into parts for the macroscopic and the microscopic description, respectively. At the first, we give the Navier-Stokes equation and the evolution equation for the composition field on the macro-scale; Subsequently, we specify the alternative approaches for calculating the stress tensor on the micro-scale involving stochastic differential equations.

2.1 Macroscopic equations

We consider the isothermal and incompressible fluid of polymer solution with density ρ. From the macroscopic viewpoint, the motion of a polymer solution fluid can be governed by the continuity and the momentum balance equation:

$$\vec{\nabla}\cdot\vec{v}=0 \tag{1}$$

and

$$\rho\frac{D\vec{v}}{Dt}=\eta_s\nabla^2\vec{v}-\vec{\nabla}p-(2\phi_A-1)\,\vec{\nabla}\mu+\vec{\nabla}\cdot\boldsymbol{\sigma}_{\mathrm{p}}(\vec{r},t) \tag{2}$$

where the material derivative $\frac{D\vec{v}}{Dt}=\frac{\partial\vec{v}}{\partial t}+\vec{v}\cdot\vec{\nabla}\vec{v}$. Involving the thermal and the viscoelastic forces, the momentum balance equation is derived using the Rayleigh's Variational Principle. For details the reader could refer to Onuki's publications[22,40]. Here ϕ_A denotes the volume fractions of the component A: the polymer solute, thus the fraction of the Newtonian solvent (component B) can be calculated as $\phi_B=1-\phi_A$. In Eqn.(2) $\vec{v}$ and p are the volume average velocity of the fluid and the pressure field, respectively. η_s represents the solvent viscosity and $\boldsymbol{\sigma}_{\mathrm{p}}$ is the time-dependent viscoelastic stress tensor contributed from the polymer dynamics. The viscoelastic stress term $\vec{\nabla}\cdot\boldsymbol{\sigma}_{\mathrm{p}}$ and the osmotic stress $\vec{\nabla}\mu$ are two significant contributions originated from the polymer chain dynamics and the thermodynamic effects, respectively. The thermodynamic effects in two-fluid framework are described through the chemical potential difference $\mu=\mu_A-\mu_B$. The chemical potentials are approximately defined in a Ginzburg-Landau scheme[40], thus μ is assumed to be the functional derivative of the mixing free energy with respect to local volume fraction as

$$\mu=\frac{\delta\mathscr{F}_{\mathrm{mix}}[\phi_A(\vec{r})]}{\delta\phi_A(\vec{r})} \tag{3}$$

We take a first order approximation of the Flory-Huggins-de Gennes mixing free energy function as

$$\mathscr{F}_{\mathrm{mix}}[\phi_A(\vec{r})]=\int d\vec{r}\left\{f_{\mathrm{mix}}+(\Gamma/2)\left[\nabla\phi_A\right]^2\right\} \tag{4}$$

and

$$f_{\mathrm{mix}}/k_{\mathrm{B}}T=(1/M_A)\,\phi_A\ln\phi_A+(1/M_B)\,\phi_B\ln\phi_B+\chi\phi_A\phi_B \tag{5}$$

where Γ is the interfacial tension coefficient, M_i is the molecular weight of each component polymer and χ is the Flory-Huggins interaction parameter.

The evolution equation for the volume fraction can be expressed as

$$\frac{D\phi_A(\vec{r},t)}{Dt}=\vec{\nabla}\cdot\left[\frac{\phi_A^2(1-\phi_A)^2}{\varsigma}\left(\vec{\nabla}\mu-\alpha\vec{\nabla}\cdot\boldsymbol{\sigma}_{\mathrm{p}}\right)\right] \tag{6}$$

which bringing the osmotic stress and the viscoelastic stress term together in the right of the equation. The parameter ς is a frictional coefficient and α is a dimensionless coefficient given by $\alpha=\frac{1}{\phi_A}$.

The chemical potential difference can be calculated from Eqn(3) and the total viscoelastic stress $\boldsymbol{\sigma}_{\mathrm{p}}$ should be obtained by solving constitutive equations. As Yuan[41] argued that the tube velocity should be used in the viscoelastic constitutive equation. The tube velocity may be expressed in terms of the volume average velocity by

$$\vec{v}_{\mathrm{T}}=\vec{v}+\phi_A(1-\phi_A)\alpha(\vec{v}_A-\vec{v}_B) \tag{7}$$

$$\vec{v}_A - \vec{v}_B = \frac{\phi_A(1-\phi_A)}{\varsigma}\left[-\vec{\nabla}\mu + \alpha\vec{\nabla}\cdot\boldsymbol{\sigma}_{\mathrm{p}}\right] \tag{8}$$

As Eqn(8) shows, the velocity difference between the component A and B depends on the thermodynamic and viscoelastic forces. In this paper, we aim to model a polymer solution where only one component (A) is viscoelastic, the tube velocity is simplified to $\vec{v}_{\mathrm{T}} = \vec{v}_A$.

2.2 Microscopic equations

On a microscopic viewpoint we set up a FENE dumbbell model for the dilute polymer solution, where the molecular chain of the polymer is considered as a suspension dumbbell consisting of two separate Brownian beads connected with an elastic spring. Using a vector $\vec{Q}$ to represent the length and the orientation of the connecting spring, the spring force can be written as the FENE form as:

$$F(\vec{Q}) = \frac{\vec{Q}}{1-|\vec{Q}|^2/b}, \qquad |\vec{Q}| \le b \tag{9}$$

where the parameter b gives the dumbbell a maximum extension.

The BCF method introduces N_f configuration fields $\vec{Q}_i(\vec{r},t)$ to replace the Fokker-Planck equation for describing the configuration distribution. We rewrite the corresponding stochastic differential equation as[31]

$$\begin{aligned} d\vec{Q}_i(\vec{r},t) = [&-\vec{v}(\vec{r},t)\cdot\nabla\vec{Q}_i(\vec{r},t) + (\nabla\vec{v}(\vec{r},t))^T\cdot\vec{Q}_i(\vec{r},t)) \\ &-\frac{F(\vec{Q}_i(\vec{r},t))}{2\lambda(\phi_A)}]dt + \sqrt{\frac{1}{\lambda(\phi_A)}}d\vec{W}_i(t) \end{aligned} \tag{10}$$

In this representation $d\vec{W}_i(t)$ only depends on time and essentially are independent Gaussian variables with zero mean and variance dt. Importantly the random variables are independent on the position $\vec{r}$. To approximate the actual probability density function, we solve Eqn.(10) for a number of stochastic realizations, represented by $\vec{Q}_i(\vec{r},t)$, $i = 1,2,\cdots,N_f$. According to the Kramers expression, the polymer contribution to the extra-stress $\boldsymbol{\sigma}_{\mathrm{p}}$ can be given by[36]

$$\boldsymbol{\sigma}_{\mathrm{p}} = (\frac{b+d+2}{b})\frac{\eta_p(\phi_A)}{\lambda(\phi_A)}(\left\langle\vec{Q}\otimes F(\vec{Q})\right\rangle - \boldsymbol{I}) \tag{11}$$

where the factor (b + d + 2)/b only needs to be multiplied for the FENE model, and d is the dimension of configuration space. Using a Monte Carlo integration, the ensemble average $\left\langle\vec{Q}\otimes F(\vec{Q})\right\rangle$ can be approximately calculated by

$$\left\langle\vec{Q}\otimes F(\vec{Q})\right\rangle \approx \sum_{i=1}^{N_f}\vec{Q}_i(\vec{r},t)\otimes F(\vec{Q}_i(\vec{r},t)) \tag{12}$$

In polymer solutions, the relaxation time λ and the polymer viscosity η_p are dependent to the concentration. Here in Eqn.(10) and Eqn.(11) we use two material functions $\lambda(\phi_A)$ and $\eta_p(\phi_A)$ to describe their relations. For simplicity, we assume a power-law dependence[42] as $\lambda(\phi_A) = \lambda^0\phi_A^{1.5}$ and $\eta_p(\phi_A) = \eta_p^0\phi_A^{2.25}$.

3 Numerical method

We use a PISO-based iterative solution algorithm to solve the multi-scale model. This algorithm has been well tested in a numerical study for the dynamics of polymer solutions in contraction flow[43]. Recently, it is adopted to study the shear-banding flows with a macroscopic two-fluid model[29]. Derived from the algorithm described in[43], the chemical potential difference unknowns and the polymer stress unknowns are both explicitly introduced into the momentum equation as source terms, therefore Eqn.(2) could be rewritten as

$$\frac{\partial\vec{v}}{\partial t} + \vec{v}\cdot\vec{\nabla}\vec{v} - \frac{\eta_s}{\rho}\nabla^2\vec{v} + \frac{(2\phi_A-1)}{\rho}\vec{\nabla}\mu - \frac{\vec{\nabla}\cdot\boldsymbol{\sigma}_{\mathrm{p}}(\vec{r},t)}{\rho} = -\frac{\vec{\nabla}p}{\rho} \tag{13}$$

After discretizing through finite volume method, this equation can be abbreviated into a form of the linear system as

$$A\vec{v}^{n+1} = H^n - \nabla[p]^n \tag{14}$$

where the brackets $[\cdot]$ represents the numerical approximation of the unknown fields,the superscript n and $n+1$ denote the value of the past and the present times of the variable. polymer stress contribution and the osmotic stress term are treated as the source terms and are contained in symbol H^n. However, the viscous term and the convective term are implicitly discretized into the matrix A of the linear system. Multiplying Eq.(14) by A^{-1} yields

$$\vec{v}^{n+1} = \vec{U}^{n+1} - A^{-1}\nabla[p]^n \tag{15}$$

where $U^{n+1} = A^{-1}H^n$ is got by taking the divergence of the Eq.(15) and applying the continuity condition in Eq.(1). We can get a Poisson equation for solving the pressure filed in the pressure-correction step:

$$\nabla\cdot\vec{U}^{n+1} = \nabla\cdot(A^{-1}\nabla[p])^{n+1} \tag{16}$$

The Eq.(15) and Eq.(16) defines the key steps for the PISO algorithm. In this paper, we replace the constitutive equation part for solving the viscoelastic stress tensor to a microscopic BCF method. A semi-implicit Euler method[39] is employed to solve the equations of the Brownian configuration fields. Combining the two parts together, we get the procedure of the iterative algorithm for solving the multi-scale two-fluid model as Algorithm **1**.

In Algorithm **1** $\vec{N}_i(0,1)$ denotes a vector containing a triple of independent Gaussian random variables with zero mean and variance one. To discretize the governing equations of the multi-scale two-fluid model, Eqn.(1) to Eqn.(12), we use an Open Source CFD toolbox released by the OpenCFD Ltd, named OpenFOAM. The equations are discretized through finite volume method, which locally satisfied the physical conservation laws through computing each term of the governing equations by integral over a control volume. For spatial discretization terms the 2nd-order Gauss MINMOD and Gauss Linear scheme are applied and the temporal terms are discretised using a simple Euler scheme. Finally these equations will reduce to linear systems, thus using the iterative solvers predefined in OpenFOAM we can get the so-

Data: Mesh data, initial conditions
Result: $\vec{v}$, p, $\boldsymbol{\sigma}_{\mathrm{p}}$, ϕ_A
read the mesh data and the initial conditions;
initialization;
while t^{n+1} *not reach the end of the simulation time* **do**
  for $i = 1$ *to* N_f **do**
    Solve Eq.(10) to get the configuration field $\vec{Q}_i(\vec{r},t)$ at time t^{n+1} using a semi-implicit Euler method: $(1+\frac{\Delta t^n}{2\lambda(\phi_A^n)(1-|\vec{Q}_i^{n+1}(\vec{r})|^2/b)})\vec{Q_i^{n+1}}(\vec{r}) = \vec{Q}_i^n(\vec{r}) + [-\vec{v^n}(\vec{r})\cdot \nabla\vec{Q}_i^n(\vec{r}) + (\nabla\vec{v^n}(\vec{r}))^T\cdot\vec{Q}_i^n(\vec{r},t))]\Delta t^n + \sqrt{\frac{\Delta t^n}{\lambda(\phi_A^n)}}\vec{N}_i(0,1)$;
  end
  Compute the polymer stress tensor using Kramers' expression $\boldsymbol{\sigma}_{\mathrm{p}}^{n+1}(\vec{r}) = (\frac{b+d+2}{b})\frac{\eta_p(\phi_A^n)}{\lambda(\phi_A^n)}(\sum_{i=1}^{N_f}\vec{Q_i^{n+1}}(\vec{r})\otimes F(\vec{Q_i^{n+1}}(\vec{r})) - \boldsymbol{I})$;
  Solve the discretised momentum equation (Eq.(13)) to obtain the estimated components $\vec{U}^{(n+1)*}$;
  Solve the pressure-correction equation (Eq.(16)) to obtain the pressure field $p^{(n+1)*}$;
  Calculate the corrected velocity field $\vec{v}^{(n+1)*}$ by solving Eq.(15);
  Repeat the steps **8** $\sim$ **10** using the corrected $p^{(n+1)*}$,$\vec{v}^{(n+1)*}$ until all corrections are negligibly small for the solutions at the present time $\vec{v}^{n+1}$ and p^{n+1};
  Solve Eq.(6) using $\boldsymbol{\sigma}_{\mathrm{p}}^{n+1}$ and $\vec{v}^{n+1}$ to obtain the volume fraction ϕ_A^{n+1};
  $n \leftarrow n+1$;
end

Algorithm 1: The iterative algorithm to solve the multi-scale two-fluid model

lutions of the equations at every time step. Typical solvers in the toolbox include the conjugate (PCG) and biconjugate gradient (PBiCG) methods. For details please refer to the OpenFOAM Manual.

4 Results and discussions

In this section we focus on the two-dimensional simulation with a simulation box in square shape, and the cell number is set to $N_{cell} = 256\times256$. The **Algorithm 1** is parallelized by a mesh-decomposition approach. In principle, all of the mesh cells are firstly decomposed into numerous parts and then distributed to different processor cores for computing. Therefore all of the sections of the algorithm are calculated in parallel.

We run the simulation on a high performance computing cluster located in the State Key Laboratory of High Performance Computing of NUDT. In this cluster each computing node contains 12 Intel Xeon E5-2620 2.10GHz CPU cores and a total main memory of 16GB. Each calculation presented in the paper costs around 2 days to 7 days on 16 CPU cores depending on the shear rates.

The top and bottom boundaries are no-slip walls and periodic boundary condition is applied to the other two sides of the simulation box. As presented in numerous previous study[27,29], care has been taken in all simulations to ensure that there are sufficient lattice sites (seven at least) across the sharpest interfaces and also that the simulation results are independent of any further refinement of lattice density.

To apply a required shear rate $\dot{\gamma}$, a velocity with the magnitude of $U_0 = \dot{\gamma}(L/2)$ is set to the top and bottom walls in equal speed and opposite directions , where L is the distance between the walls. Other parameters remain constant throughout all of the simulations and are set as shown in Table 1 :

Table 1 Parameters used in simulations

Parameter	Value
η_s	0.1
$k_{\mathrm{B}}T$	1.3
M_A	1.0
M_B	1.0
Γ	1.0
ς	0.1
b	20.0
λ^0	10.0
η_p^0	20.0

For this set of parameters, the critical point is at $(\chi = 2.0, \phi_A^0 = 0.5)$ as shown in Fig. 1. By changing the value of χ and the initial volume fraction ϕ_A^0, different regions in the phase diagram can be explored. For simplicity, in this paper we fix the initial volume fraction $\phi_A^0 = 0.5$ for studying a symmetric binary fluid and $\phi_A^0 = 0.3$ for a asymmetric case.

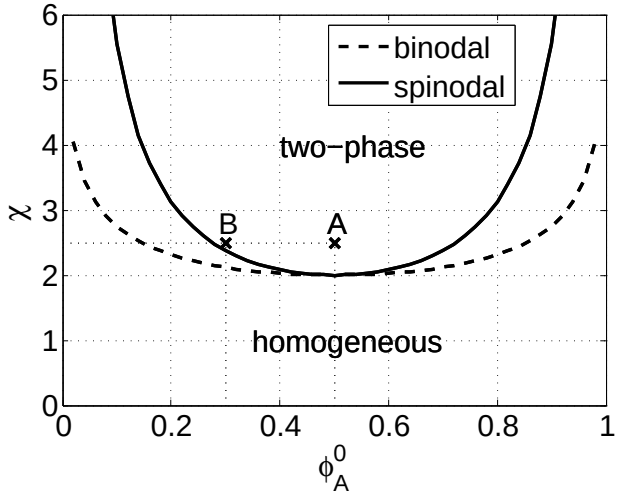

Fig. 1 Equilibrium phase diagram of Flory-Huggins free energy with parameters: $M_A = M_B = 1.0$ and $k_BT = 1.3$. The homogeneous and two-phase fluid areas are bordered by binodal and spinodal lines, and between the two is a metastable region. The two bold crosses marked the parameters used in this paper: A: $(\phi_A^0, \chi) = (0.5, 3.0)$ and B: $(\phi_A^0, \chi) = (0.3, 3.0)$

In the simulations, we employ the 2D FENE dumbbell model to predict the viscoelastic stress of a shear-shinning fluid. Compared to the simple Hookean dumbbell model, the extensibility parameter b controls the fluid's shear thinning behaviour. As shown in numerous publications[39,44,45], the steady-state numerical results of the stress varied significantly by changing the value of b. To give a preliminary validity of the numerical scheme presented in Section 3, we perform the steady shear flow simulations with fixed Weissenberg Number $W_e = \dot{\gamma}\lambda \in [1, 10^3]$, and by setting the cell number of the mesh $N_{cell} = 1$ the spatial discretization is ne-

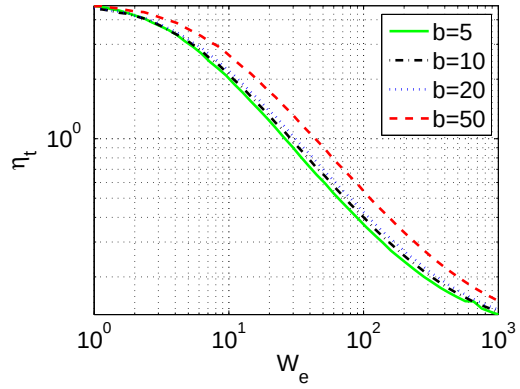

(a) $\eta_t = \eta_s + \eta_p$

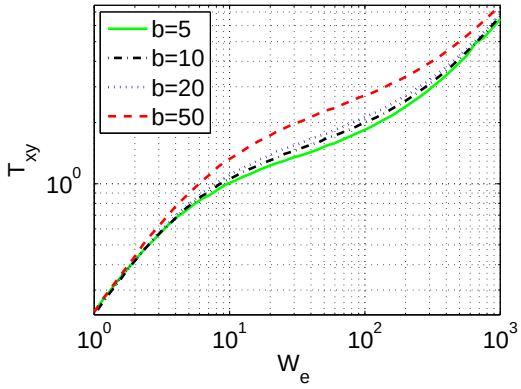

(b) T_{xy}

Fig. 2 The scaled steady-state shear stress (scaled by $\frac{\eta_p^0}{\lambda^0}$) and the total viscosity over W_e with $b = 5, 10, 20, 50$ for $N_f = 50000$

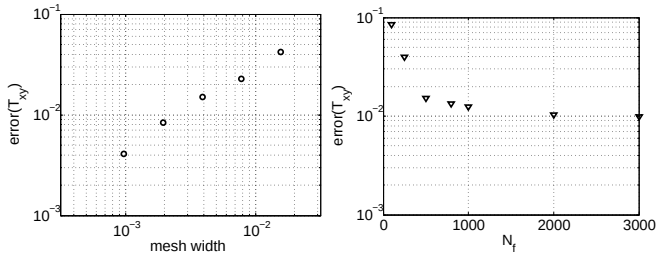

(a) Error vs. mesh width for $N_f = 500$ (b) Error vs. N_f for $N_{cell} = 256^2$

Fig. 3 The convergence study with different mesh width and number of configuration fields. The $error(T_{xy})$ is calculated through the steady-state truncation error of the shear stress normalized by the results for $N_{cell} = 1$.

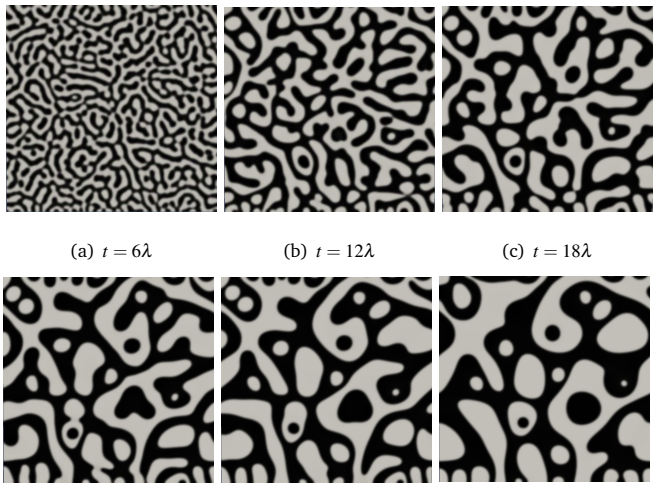

(a) $t = 6\lambda$ (b) $t = 12\lambda$ (c) $t = 18\lambda$

(d) $t = 24\lambda$ (e) $t = 30\lambda$ (f) $t = 42\lambda$

Fig. 4 Time series of phase separation after a deep quench into the spinodal region through the symmetric initial composition $\phi_A^0 = 0.5$ and $\chi = 2.5$

glected. For fixed W_e, each simulation evolved $N_f = 50000$ Brownian Configuration fields until a steady state is reached. Thus we can measure the resulting stresses and finally give the value of the total viscosity of the fluid η_t and the shear stress for corresponding W_e.

The results are presented in Fig. 2. The viscosity η_t in Fig. 2(a) decreases with W_e increasing. This typical shear-shining behaviour was observed experimentally in polymer solutions[46] and compared numerically using a macroscopic PTT constitutive model and a multi-scale model coupling the BCF scheme[39]. The corresponding constitutive curves are presented in Fig. 2(b). All the curves follow similar trends and the larger extensity lead to greater stresses as shown in the results. In practice the maximum Weissenberg number achievable reduces as b increasing. As pointed by Chauviere[44], increased b means that the configuration domain becomes larger, therefore more refined meshes would be necessary in order to capture localized features. We choose a moderate value of the extensity $b = 20$ for all the simulations below.

For the convergence study, we compared the simulation results with the steady-state solutions in Fig. 2 under different mesh width and various number of configuration fields N_f. The time step size is restricted by the CFL condition $\Delta t \leq \Delta x/|u_{max}|$ in our simulations. The results are presented in Fig. 3. For a constant $N_f = 500$, the truncation error for the steady-state shear stress is linearly decreased as increasing the number of cells. Differently, with a fixed mesh size $N_cell = 256^2$, the error is rapidly reduced to around 10^{-2} as N_f increased to 500, however there is no significant variation from $N_f = 500$ to $N_f = 3000$. Considering the massive computing resource requirements for large N_f, we choose $N_f = 500$ for all the simulations presented below.

Without shear flow, the phase separation will spontaneously take place after a deep temperature quench and the fluid will form into two-phase state driven by the thermodynamical forces. the asymmetry between the components of polymer mixtures can also strongly change the morphology of phase separation[41,47]. Typically, in the zero-shear system an asymmetric quench can lead to a droplet pattern, other than the bicontinuous pattern for a nearly symmetric quench[48]. In order to reproduce the spinodal decomposition process in a zero-shear system, we carry out two sets of simulations with symmetric initial composition $\phi_A^0 = 0.5$ and asymmetric initial composition $\phi_A^0 = 0.3$, respectively. The time series of the numerical results are presented in Fig. 4 and

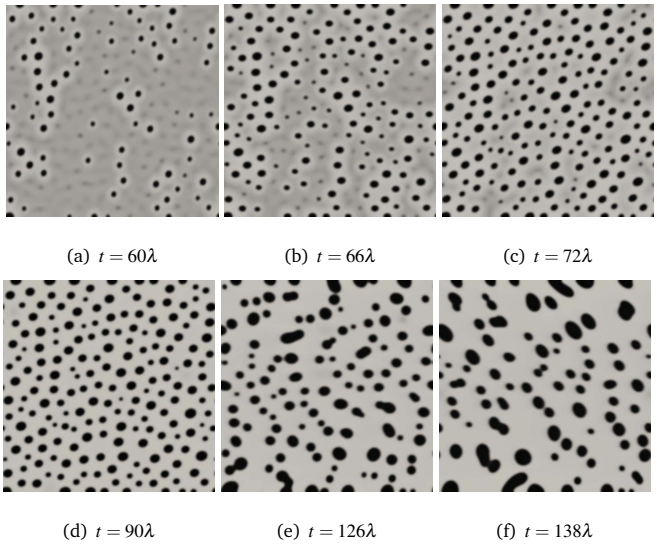

Fig. 5 Time series of phase separation after a deep quench into the spinodal region at an asymmetric initial composition $\phi_A^0 = 0.3$ and $\chi = 2.5$

Fig. 5.

Fig. 4 shows the snapshots of the composition field ϕ_A for the critical quench $\phi_A^0 = 0.5$. At $t = 6\lambda$, the clearly isotropic bicontinuous domain structure has been formed and the difference between the two phases grows as the phase separation proceeds. The coarsening of the morphology structure with time can be clearly seen from the plots. After $t = 50\lambda$, the finite-size effects can not be eliminated and therefore the full hydrodynamic regime is not obtainable. Fig. 5 is the time series of snapshots for the asymmetric case with $\phi_A^0 = 0.3$. Differently, the polymer-rich phase (component A) forms a dispersed droplet structure. As simulation proceeds, the smallest droplets dissolve completely into the continuous solvent phase and the larger droplets merge together, thus the average size of the droplets increases with time.

From a microscopic viewpoint, we plot the polymer configurations at the position (64, 64) in Fig. 6 . After visualizing the configuration vectors in Fig. 6(a), the probability density function (PDF) for the squared distance $\vec{Q}^2$ which is limited by $b = 20$ is calculated. From the plots it is clear that most of the configurations are in an equilibrium state in the absence of flow and no significant molecule extension is found as shown in Fig. 6(b).

For the cases with the fluid under different flow rates, firstly we plot the simulation results for the homogeneous cases($\chi = 1.0, \phi_A^0 = 0.5$) and the two-phase cases ($\chi = 2.5, \phi_A^0 = 0.5$) in Fig. 7, along with the corresponding steady-state shear stress with $N_{cell} = 1$. For this set of parameters, the constitutive curve calculated from the microscopic Brownian configurations is strictly monotonic as indicated in Fig. 7. Additional for a homogeneous case, the simulation results using the numerical algorithms described in Section 3 are coincide well with the steady-state calculations. Whilst the phase separation occurs by changing the parameter $\chi = 2.5$, the calculated shear stresses are markedly smaller than the homogeneous cases. This observation is coincide with the numerical results based on a macroscopic constitutive model[29]. We also tested different number of the Brownian

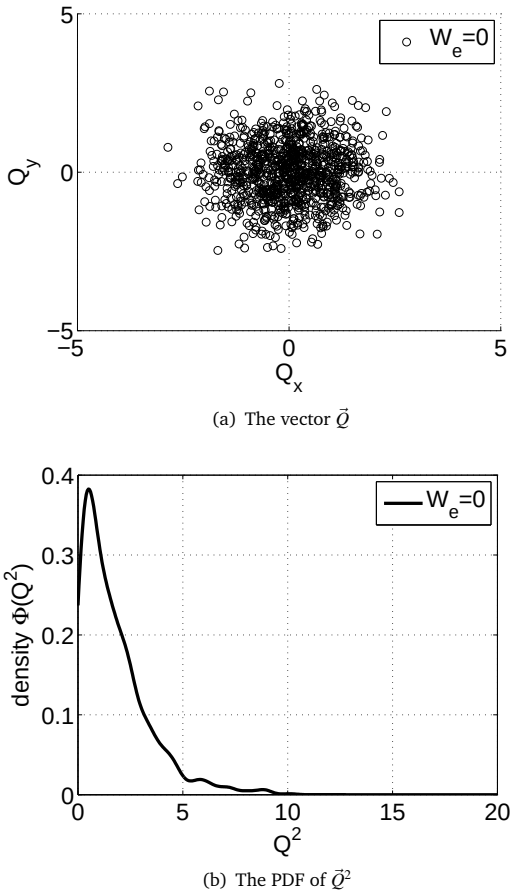

Fig. 6 The distribution of the configuration vectors sampled at the position (64, 64) with $N_f = 500$ in a zero-shear system

configurations , and it is observed that larger N_f will bring higher accuracy for the calculations. Considering the simulation time cost, we choose $N_f = 500$, and it is found the results are generally satisfactory as shown in Fig. 7.

By applying the shear flow, the phases will be rapidly elongated and form into band structures. As shown in Fig. 8 for the case of $W_e = 20.0$, snapshots of the composition field at several instants during the spinodal phase separation give us the detailed information for the microstructure evolution driven by the thermodynamics, hydrodynamics and the viscoelasticity. At the beginning point, $t = 0$, the fluids are defined on a completely homogeneous volume fraction plus a small amplitude Gaussian random noise with an intensity of 10^3. As shown in Fig. 8(b)-8(c), shear bands emerge rapidly and become coarser through a diffusive mechanism. After $t = 5.4\lambda$, the wavy structures between the bands have become extremely unstable and began to evolve in a chaotic manner. At later times presented in Fig. 8(g)-8(l) , it is observed that wavy structures break up to form droplets,then the droplet interacts with the remaining bands and subsequently forms into a coarser band. In overall, the dynamical mechanisms by which the shear bands reach to a steady state are analogical to the phenomena reported in thermodynamical equilibrium shear-banding systems[27,29,41]. One is the diffusive mechanism and the another is the convective through wave instability. By introducing the ther-

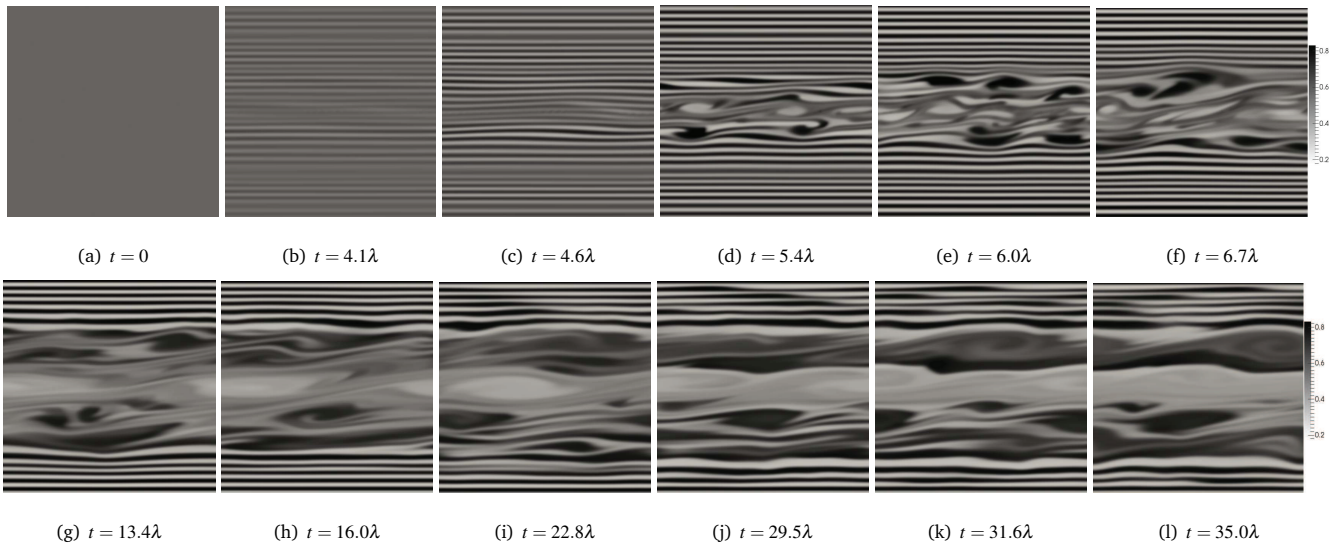

Fig. 8 The snapshots of the composition field of the polymer component at various times t, scaled by the relaxation time λ for the case of $W_e = 20$

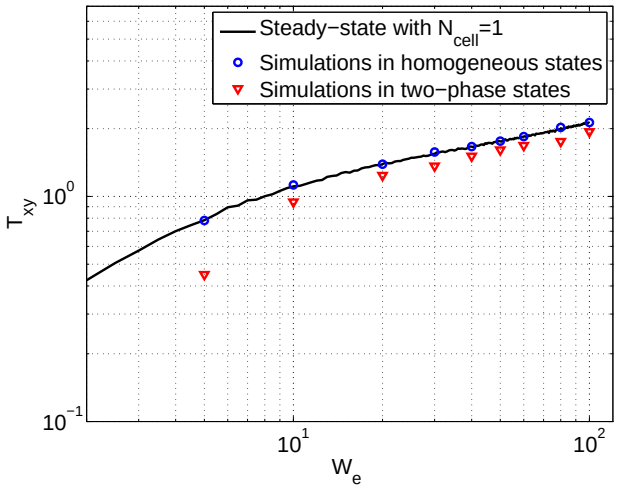

Fig. 7 The scaled steady-state shear stress with $N_{cell} = 1, N_f = 5 \times 10^4$ and the simulation results for the homogeneous cases($\chi = 1.0, \phi_A^0 = 0.5$) and the two-phase cases ($\chi = 2.5, \phi_A^0 = 0.5$) under different flow rates with $N_f = 500$

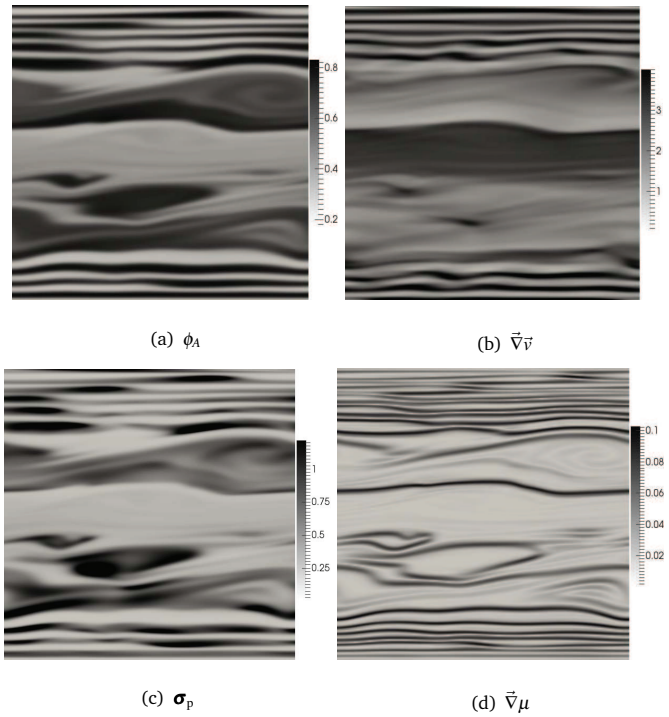

Fig. 9 The snapshots of field variables at the same time $t = 35\lambda$

modynamical forces in a two-phase region of the phase diagram, the shear bands are becoming much more unstable and can not reach a steady state for a long simulation time.

It is clear that the phase separation is directly linked to the rheological properties of the fluid and the applied flow field. As presented in Fig. 9, the evolution of the gradient of the velocity field and the stress field follow the similar patterns as that of the composition field. In Fig. 9(b) and Fig. 9(c), the $\vec{\nabla}\vec{v}$ and $sigp$ form into the similar band structures as Fig. 9(a) at $t = 35\lambda$. From Fig. 9(d), we can tell that the osmotic pressure field $\vec{\nabla}\mu$ introduces a interfacial force concentrating at the narrow interfaces between the polymer-rich region and the solvent-rich region.

To explore the distribution of the molecule configurations under different shear flows, we record the configuration fields at the lattice point (64, 64) for four different Weissenberg numbers. As shown in Fig. 10, the corresponding PDF calculations have also been plotted in the right column of the figure. For the case with a low shear rate $W_e = 5$, the molecule chains are obviously elongated compared to the zero-shear case shown in Fig. 6. In absence of the flow, most of configurations are restricted in the range of $\vec{Q}^2 < 5$, yet in Fig. and 10(a) and 10(b) a considerable amount of the molecules have been stretched and the measurement of $\vec{Q}^2$ increased into the range of $[5, 10]$. Under a much higher shear flow for $W_e = 120$ shown in Fig. 10(g) and 10(h), most of the sampled molecules are extremely elongated close to their maximum

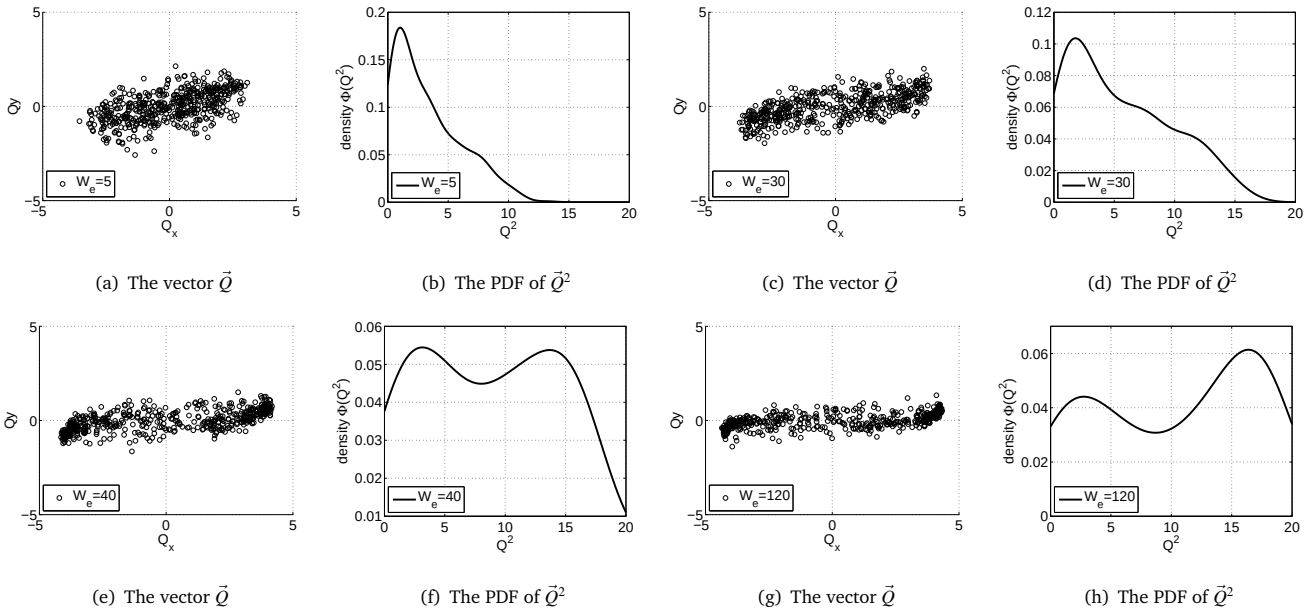

(a) The vector $\vec{Q}$ (b) The PDF of $\vec{Q}^2$ (c) The vector $\vec{Q}$ (d) The PDF of $\vec{Q}^2$

(e) The vector $\vec{Q}$ (f) The PDF of $\vec{Q}^2$ (g) The vector $\vec{Q}$ (h) The PDF of $\vec{Q}^2$

Fig. 10 The distribution of the molecule configurations with $N_f = 500$ under different shear flows at the lattice point (64,64)

as $10 < \vec{Q}^2 < 20$. From the plots for four different Weissenberg numbers, we obtain a typical shear flow pattern for both flows as the higher shear flows leading to stronger molecule extensions.

5 Conclusions

The phase transitions under flow have been extensively studied experimentally and numerically over the last decades, nevertheless, due to the massive computational requirements, there are still no multi-scale numerical studies that give a linkage between the microscopic molecule configurations to the macroscopic morphological transitions in a multi-phase fluids under flow. As a coarse-grained microscopic approach, the Brownian Configuration Fields(BCF) method makes it possible to model the macroscopic phenomena of complex fluid on a microscopic viewpoint.

In this paper, we couple the BCF method in a two-fluid framework to model the phase transition under shear flow in dilute polymer solutions. The governing equations are solved using a modified PISO iterative algorithm based on the finite volume scheme. Based on necessary validations, 2D simulation results of non-equilibrium phase transition after a temperature quench under shear flow are presented and analyzed. On a macroscopic viewpoint, we give the time series of the morphological evolution of the macroscopic variable fields, and the results reproduce many dynamic phenomena reported in literature, including the spinodal decomposition, the interface instabilities between the shear bands, and the dynamic mechanisms to reach coarser band structures. On a microscopic viewpoint, the distribution of the molecule configurations in the simulation box could be observed as the phase transition taking place. The underlying configuration fields are recorded and the corresponding PDFs are analyzed under various flow rates.

The multi-scale two-fluid model presented here provides a possible approach to numerically study the multi-phase viscoelastic fluids under flow. In the future, this model could be used to quantitatively study some outstanding problems by appropriately selecting the parameters base on the experimental observations. Furthermore, we will optimize the parallel algorithms to significantly reduce the computational costs.

Acknowledgments

The authors would like to thank Prof. Xue-Feng Yuan for helpful discussions, the National Natural Science Foundation of China (Grant No.61221491, No.61303071 and No. 61120106005), and the Open fund from State Key Laboratory of High Performance Computing (No. 201303-01, 201503-01 and 201503-02) for funding.

References

1 A. Silberberg and W. Kuhn, *Nature*, 1952, **170**, 450–451.
2 S. Ravindranath, S. Q. Wang, M. Olechnowicz, V. S. Chavan and R. P. Quirk, *Rheologica Acta*, 2011, **50**, 97–105.
3 S. Lerouge and J. F. Berret, *Polymer Characterization: Rheology, Laser Interferometry, Electrooptics*, 2010, **230**, 1–71.
4 M. Laurati, G. Petekidis, N. Koumakis, F. Cardinaux, A. B. Schofield, J. M. Brader, M. Fuchs and S. U. Egelhaaf, *Journal of Chemical Physics*, 2009, **130**, 134907.
5 B. Lonetti, M. Camargo, J. Stellbrink, C. N. Likos, E. Zaccarelli, L. Willner, P. Lindner and D. Richter, *Physical Review Letters*, 2011, **106**, 228301.
6 P. D. Olmsted, *Rheologica Acta*, 2008, **47**, 283–300.
7 S. Manneville, *Rheologica Acta*, 2008, **47**, 301–318.
8 J. K. G. Dhont and W. J. Briels, *Rheologica Acta*, 2008, **47**, 257–281.
9 P. T. Callaghan, *Rheologica Acta*, 2008, **47**, 243–255.
10 P. Guenoun, R. Gastaud, F. Perrot and D. Beysens, *Physical Review A*, 1987, **36**, 4876–4890.

11 C. K. Chan, F. Perrot and D. Beysens, *Physical Review A*, 1991, **43**, 1826–1839.

12 T. Hashimoto, K. Matsuzaka, E. Moses and A. Onuki, *Physical Review Letters*, 1995, **74**, 126–129.

13 J. Lauger, C. Laubner and W. Gronski, *Physical Review Letters*, 1995, **75**, 3576–3579.

14 K. Matsuzaka, T. Koga and T. Hashimoto, *Physical Review Letters*, 1998, **80**, 5441–5444.

15 F. Corberi, G. Gonnella and A. Lamura, *Physical Review Letters*, 1999, **83**, 4057–4060.

16 Z. Y. Shou and A. Chakrabarti, *Physical Review E*, 2000, **61**, R2200–R2203.

17 L. Berthier, *Physical Review E*, 2001, **63**, 051503.

18 H. Lowen, *Journal of Physics-Condensed Matter*, 2008, **20**, 404201.

19 P. Stansell, K. Stratford, J. C. Desplat, R. Adhikari and M. E. Cates, *Physical Review Letters*, 2006, **96**, 085701.

20 K. Stratford, J.-C. Desplat, P. Stansell and M. Cates, *Physical Review E*, 2007, **76**, 030501.

21 S. M. Fielding, *Physical Review E*, 2008, **77**, 021504.

22 M. Doi and A. Onuki, *Journal De Physique Ii*, 1992, **2**, 1631–1656.

23 S. T. Milner, *Physical Review E*, 1993, **48**, 3674–3691.

24 H. Ji and E. Helfand, *Macromolecules*, 1995, **28**, 3869–3880.

25 N. Clarke and T. C. B. McLeish, *Physical Review E*, 1998, **57**, R3731–R3734.

26 S. M. Fielding and P. D. Olmsted, *Physical Review Letters*, 2003, **90**, 224501.

27 L. Jupp, T. Kawakatsu and X. F. Yuan, *Journal of Chemical Physics*, 2003, **119**, 6361–6372.

28 S. M. Fielding and P. D. Olmsted, *Physical Review Letters*, 2006, **96**, 104502.

29 X.-W. Guo, S. Zou, X. Yang, X.-F. Yuan and M. Wang, *RSC Advances*, 2014, **4**, 61167–61177.

30 R. Keunings, *Rheology reviews*, 2004, **2004**, 67–98.

31 M. Hulsen, A. Van Heel and B. Van Den Brule, *Journal of Non-Newtonian Fluid Mechanics*, 1997, **70**, 79–101.

32 H. ÃŰttinger, B. Van Den Brule and M. Hulsen, *Journal of non-newtonian fluid mechanics*, 1997, **70**, 255–261.

33 X. J. Fan, N. Phan-Thien and R. Zheng, *Journal of Non-Newtonian Fluid Mechanics*, 1999, **84**, 257–274.

34 M. Bajaj, P. P. Bhat, J. R. Prakash and M. Pasquali, *Journal of Non-Newtonian Fluid Mechanics*, 2006, **140**, 87–107.

35 Z. M. Lu, B. C. Khoo, H. S. Dou, N. Phan-Thien and K. S. Yeo, *Chemical Engineering Science*, 2006, **61**, 4998–5009.

36 X. Y. Xu, J. Ouyang, W. M. Li and Q. S. Liu, *Journal of Non-Newtonian Fluid Mechanics*, 2014, **208**, 59–71.

37 T. N. Phillips and K. D. Smith, *Journal of Non-Newtonian Fluid Mechanics*, 2006, **138**, 98–110.

38 C. Mangoubi, M. A. Hulsen and R. Kupferman, *Journal of Non-Newtonian Fluid Mechanics*, 2009, **157**, 188–196.

39 M. Griebel and A. Ruttgers, *Journal of Non-Newtonian Fluid Mechanics*, 2014, **205**, 41–63.

40 A. Onuki, *Journal of Physics: Condensed Matter*, 1997, **9**, 6119.

41 L. Jupp and X. F. Yuan, *Journal of Non-Newtonian Fluid Mechanics*, 2004, **124**, 93–101.

42 M. Cromer, M. C. Villet, G. H. Fredrickson and L. G. Leal, *Physics of Fluids*, 2013, **25**, 051703.

43 S. C. Omowunmi and X. F. Yuan, *Rheologica Acta*, 2013, **52**, 337–354.

44 C. Chauviere and A. Lozinski, *Journal of Non-Newtonian Fluid Mechanics*, 2004, **122**, 201–214.

45 A. Lozinski and U. Chauviere, *Journal of Computational Physics*, 2003, **189**, 607–625.

46 P. C. Sousa, P. M. Coelho, M. S. N. Oliveira and M. A. Alves, *Chemical Engineering Science*, 2011, **66**, 998–1009.

47 H. Tanaka, *Journal of Chemical Physics*, 1994, **100**, 5323–5337.

48 H. Tanaka, *Journal of Chemical Physics*, 1996, **105**, 10099–10114.